RESEARCH PAPER

# Distribution of the low velocity bulk in the middle-to-lower crust of southern Tibet: implications for formation of the north–south trending rift zones

**Mingming Jiang · Yinshuang Ai · Shiyong Zhou ·
Yongshun John Chen**

**Abstract**   We conducted the ambient noise tomography to image the shallow crustal structure of southern Tibet. The 2D maps of phase velocity anomalies at the periods of 10–16 s show that the low velocities are mainly confined along or near some of the rift zones. While the maps at the periods of 18–25 s show that the coherent patterns that the low velocities expand outside of the rift zones. It means that the low velocities are prevailing in the middle crust of southern Tibet. According to the previous study of surface wave tomography with teleseismic data, we find that the low velocities from the lower crust to the lithospheric mantle are also restricted to the same rift zones. Thus, the integrated knowledge of the distribution of the low velocities in southern Tibet provides some new insight on the formation of the north–south trending rift zones. Compiling the multidiscipline evidences, we conclude that the rifting was an integrated process of the entire lithosphere in the early stage ($\sim$ 26–10 Ma), but mainly occurred within the upper crust due to the weakening a decoupling in the low velocity middle crust in the late stage (later than $\sim$ 8 Ma).

**Keywords**   Ambient noise tomography · Southern Tibet · North–south trending rift zones

M. Jiang · Y. Ai (✉)
Key Laboratory of the Earth's Deep Interior, Institute of Geology and Geophysics, Chinese Academy of Sciences, Beijing 100029, China
e-mail: ysai@mail.iggcas.ac.cn

S. Zhou · Y. J. Chen
Institute of Theoretical and Applied Geophysics, School of Earth and Space Sciences, Peking University, Beijing 100871, China

## 1 Introduction

While there is a general consensus that partial melting inferred by low seismic velocities (Brown et al. 1996; Makovsky et al. 1996; Nelson et al. 1996) and low electric resistivity (Wei et al. 2001; Unsworth et al. 2005) is present in the crust of southern Tibet, how the weak and hot materials related to partial melting distribute have been a focus of continual debate (e.g., Hung et al. 2010). This topic is further linked to whether and how the crustal channel flows exist. Many tectonic models have been proposed to explain upward extrusion and exhumation of middle-to-lower crustal materials including the emplacement of post-tectonic granites along the Himalayas, and eastward extension of Tibet based on the assumption of channel-like flows of a weak, ductile middle-to-lower crust (Beaumont et al. 2004; Royden et al. 2008). Thus, the position and shape of the low seismic velocity bulks in the crust of southern Tibet are a key to solve the dynamic process of Indian–Eurasian collision.

To delineate the distribution of low velocities in the crust is a typical 3D-imaging problem in nature. However, the previous studies yielded the images mainly along the active rift zones in southern Tibet because of the limited conditions of the observations (Brown et al. 1996, Nelson et al. 1996, Unsworth et al. 2005). Their conclusions of a pervasive partial melting in the middle crust of southern Tibet were also disputed. For instance, Hung et al. (2010) used the seismic data collected by a 2D array of Project Hi-CLIMB to image the 3D lithospheric structure of southern Tibet with a new body wave tomography method. They found that the observed low velocity bulks were not interconnected in the lower crust and concluded that there might be no pervasive partial melting in the crust of southern Tibet. As we know, body wave tomography is not

suitable to provide sufficient resolution to the shallow structure of the Earth. For the very thick crust ($\sim 75$ km) of southern Tibet, body wave tomography cannot provide reliable information of the upper and middle crust. Therefore, it is still unknown whether the low velocities and the related partial melting are pervasive or not.

Surface wave tomography is a powerful tool to detect the structure of entire lithosphere. Due to the paucity of data, only a few studies of surface wave dispersion analysis were conducted in southern Tibet. For instance, Cotte et al. (1999) found the difference of crustal structure between north and south of the Indus-Tsangpo Suture zone (ITS) in southern Tibet by dispersion and amplitude analysis of teleseismic Rayleigh waves using the INDEPTH II data; Rapine et al. (2003) measured the surface wave dispersions of five earthquakes recorded by the INDEPTH III array and revealed the very different crustal structures between southern and central Tibet. Combining ambient noise tomography and surface wave tomography with teleseismic data is an advanced and popular procedure to image the lithospheric structure of full depth range and high resolution (Yao et al. 2006, 2008; Yang et al. 2008). In this paper, we perform the ambient noise tomography. Compiling the results of ambient noise tomography and our previous two-plane wave earthquake tomography (Jiang et al. 2011), we discuss the distribution of partial melting and the formation of the north–south trending rift zones in southern Tibet.

## 2 Data and method

The seismic data used in this paper were collected by the international collaborative Hi-CLIMB project. The seismic array deployed consisted of two parts: the main north–south trending linear array and the complementary 2D regional array. The operating period was from July 2004 to August 2005 (Nábelek et al. 2009). To establish a 3D structure of the crust, we primarily used the data of the 2D complementary array and added 5 stations out of the main array. Thus, the study region was located in the Lhasa block and the Tethyan Himalayas across the ITS (Fig. 1b). This area was a blank of previous studies between the linear Hi-CLIMB main array and the INDEPTH array and its southernmost part overlapped the HIMNT array (Fig. 1a). The selected array spanned $\sim 500$ km in east–west direction and $\sim 300$ km in north–south direction with the average station interval of $\sim 25$ km.

The processing procedure of ambient noise adopted here is similar to that described in details by Bensen et al. (2007). In order to measure the dispersion of Rayleigh waves, we first decimated continuous raw data of vertical component to one sample per second, cut them into segments of a-half-day long, and normalized the instrumental
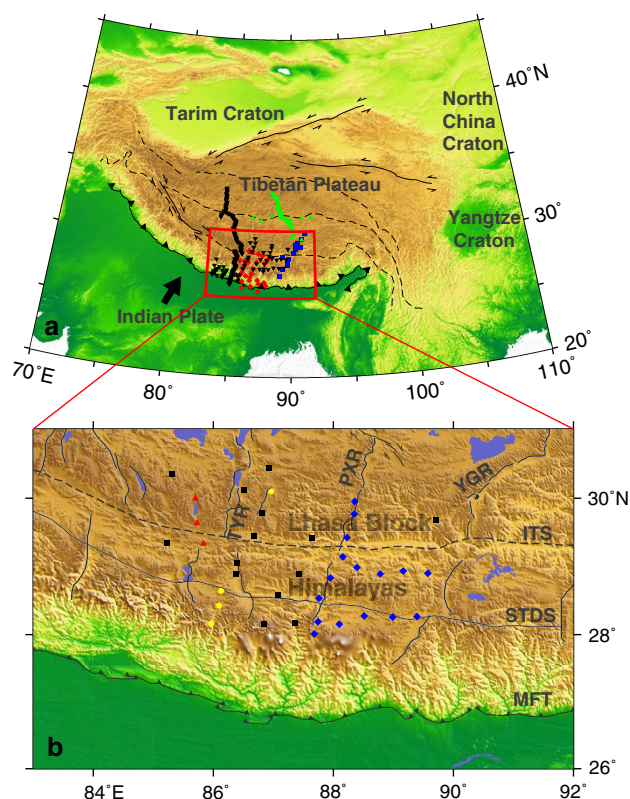


**Fig. 1** Geographic position (**a**) and Topographic map (**b**) of the study region in the southern Tibet. **a** The study region is delineated by the *open box*, and the seismic arrays deployed by INDEPTH II, INDEPTH III, HIMNT, and Hi-CLIMB are shown with *blue squares*, *green triangles* and *red diamonds*, *black inverse triangles*, respectively. The seismic array used in this paper is a part of Hi-CLIMB array (*black inverse triangles*), which consists of the 2D complementary array and added five stations out of the main array. **b** The seismic array used in this paper is marked with different types of stations by different symbols: *black squares* denote stations with the STS-2 sensors, *red triangles* denote stations with the CMG-3T sensors, *blue diamonds* denote stations with the CMG-3ESP sensors, and *yellow circles* denote stations with the Trillium-40 sensors. The main tectonic boundaries and the N–S trending rifts are shown as follows: *MFT* Main Frontal Thrust, *STDS* Southern Tibet Detachment System, *ITS* Indus-Tsangpo Suture, *TYR* Tangra Yum Co rift, *PXR* Pumqu-Xianza rift, and *YGR* Yadong-Gulu rift

responses to same type (STS-2 sensor and RT72A DAS). Then, removal of mean and linear trend and a bandpass filter of 5–50 s were applied to the data. To suppress the signals of earthquakes, the running absolute mean normalization in the time domain was applied. To extend the spectral contents, spectral whitening by a similar normalization in the spectral domain was also applied. After processing the single station data, cross-correlation functions were calculated between each station pair and stacked over $\sim 13$ months from July 2004 to August 2005. The resultant cross-correlation functions were checked based on signal-to-noise ratio (SNR), station interval, and data consistency. We defined the maximum amplitude of the

Rayleigh waveform as the signal value. The Rayleigh waveform was cut depending on its group velocity. The noise value was defined by the RMS amplitude of 100-s-long waveform just following the signal window. The SNR was the signal value divided by the noise value. The criteria of SNR and station interval were 10 and three wavelength for individual period, respectively. The data consistency was checked by comparing the moveout of related traces (Fig. 2). The final dataset and the average SNR at the period of 8–29 s are shown in Fig. 3. Considering the average SNR and numbers of seismographs at each period, we only perform 2D tomography for the periods of 10–25 s.

According to the theoretical work under the homogenous source distribution assumption (e.g., Lobkis and Weaver 2001; Roux et al. 2005), the empirical Green's function (EGF) $G_{AB}$ between stations A and B can be related to the ambient noise cross-correlation function $C_{AB}$ as follows:

$$\frac{dC_{AB}(t)}{dt} = -G_{AB}(t) + G_{BA}(-t), \quad -\infty \leq t < \infty \quad (1)$$

After averaging the positive and negative parts of cross-correlation function, we obtain the "symmetric signal" and the relationship with the EGF:

$$G_{AB}(t) = -\frac{d}{dt}\left[\frac{C_{AB}(t) + C_{AB}(-t)}{2}\right], \quad 0 \leq t < \infty \quad (2)$$

In practice, the EGFs are not necessary for measuring the phase velocities. The automated frequency time analysis was used to measure the dispersion curve of Rayleigh waves (Levshin et al. 1989; Bensen et al. 2007). We directly measured symmetric cross-correlation functions for group velocities and further calculated the phase velocities with a reminder of a π/2 phase shift from cross-correlation functions to EGFs (Bensen et al. 2007).

2D surface wave tomography was applied on the resultant dispersion measurements to yield Rayleigh wave phase velocity maps on a 0.25° by 0.25° grid. The tomographic code used was developed by Barmin et al. (2001). Damping was automatically applied depending on local path density and smoothing was applied with the spatial smoothing length of 50 km. The relative weights of smoothing term and damping term to the misfit are 200 and 0.5, respectively. Before determining these final regularization parameters, we have tested different parameters and have compared the inversion results empirically. We also delineated the reliable area for the inversions depending on the coverage of data (Fig. 4). The phase velocities outside the reliable area were automatically tapper off to the average phase velocities of the study region.
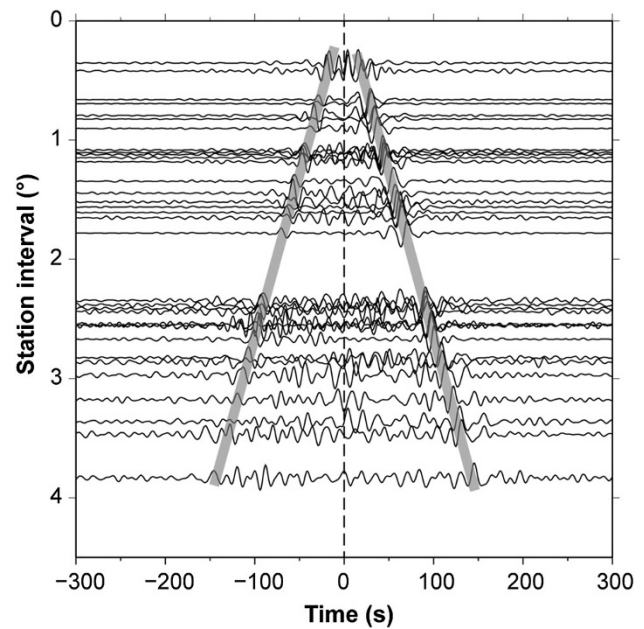


**Fig. 2** The 5–50 s bandpass filtered vertical–vertical cross-correlation record section centered at station T008 (southeastern corner of the 2D array). The *thick gray lines* indicate the approximate moveout
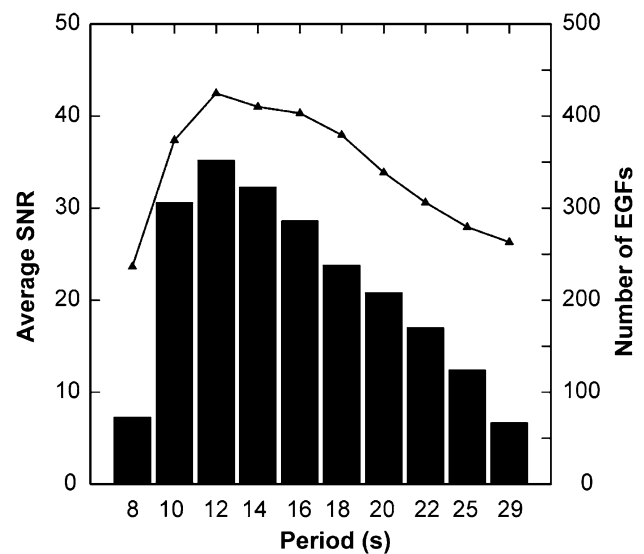


**Fig. 3** Average SNR (*black curve* with *triangles*) and numbers (*black bars*) of EGFs used for 2D phase velocity tomography. Only station pairs separated by a distance greater than three wavelength are used

## 3 Results

The average phase velocities of the study region in southern Tibet at the periods of 8–142 s are shown in Fig. 5a. The phase velocities at the short periods of 8–29 s are resulted from ambient noise tomography, and those at the long periods of 25–142 s are the previous results of two-plane wave tomography (Jiang et al. 2011). As southern Tibet is an active orogenic
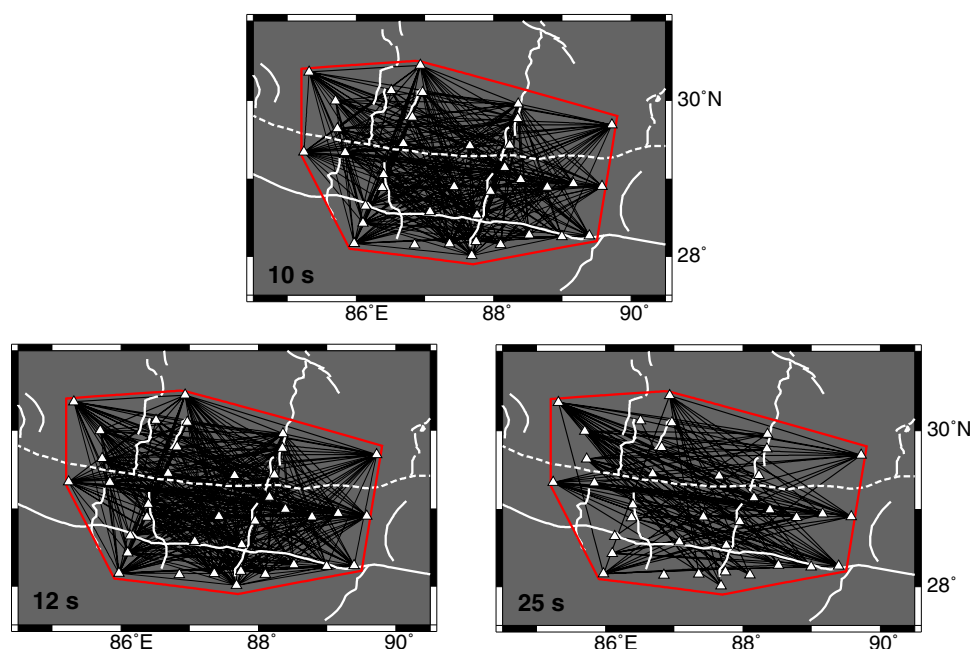
**Fig. 4** Great *circle* ray path coverage at the period of 10, 12, 25 s. The *area* delineated by *red lines* is the reliable zone in the 2D phase velocity tomography. The main tectonic boundaries and the N–S trending rifts are marked as same as in Fig. 1

belt, the resultant phase velocities are far lower than the global averages (Kennett et al. 1995). On the other hand, the phase velocities at the overlapping periods of 25–29 s between two surface wave tomography methods are very consistent (Fig. 5b). It supports that the results in this paper and the previous study of two-plane wave tomography are reliable.

Considering the relative low average SNR (<30) and few available data (<100), we did not invert the 2D phase velocity maps for the periods of 8 and 29 s. Maps of 2D phase velocity anomalies at the periods of 10–25 s are shown in Fig. 6. Velocity anomalies are calculated relative to the average velocities of the study region (Fig. 5). According the synthetic calculation, the phase velocity at an individual period is mainly sensitive to the structure at the depth of one third of the related wavelength (Fig. 7). The low velocities at the periods of 10–16 s are consistently confined to the Tangra Yum Co rift zone in the west and near the Yadong-Gulu rift zone in the east. This may reflect that the low velocity bulks in the upper crust (∼10–20 km) of southern Tibet are not interconnected. As the period increases (16–25 s), the spatial contents of the low velocities expand outside of the rift zones. Low velocities are observed prevailing in the mid-crust (∼20–40 km) of the southern Tibet.

The common resolution distance of ambient noise tomography within the reliable area is ∼50 km for such a kind of seismic array of ∼25-km interstation distance used in this paper (e.g., Yang et al. 2008). Checker board tests are also conducted to check the resolution. The input velocity anomalies are ±3 % relative to the average phase velocities

with the size of 1° × 1°. Our test results show that the patterns of the checker board can be recovered at all periods within the reliable area, but the amplitudes of velocity anomalies are only partly recovered (Fig. 8). Another way to test the reliability of ambient noise tomography is to compare the results with those of surface wave tomography with teleseismic data. Comparison of the results between ambient noise tomography and two-plane wave tomography using the data from the same array is shown in Fig. 9. At the overlapped period of 25 s, the patterns of phase velocity anomalies are fairly consistent in the overlapped reliable area of two tomographic studies. The differences of the amplitudes of anomalies may be due to different datasets and tomography methods. From the comparison, we conclude that the 2D phase velocity maps in this paper are reliable.

## 4 Discussion

Observations of low seismic velocities (Kind et al. 1996; Nelson et al. 1996; Hung et al. 2010) accompanying with low electric resistivity (Pham et al. 1986; Chen et al. 1996; Wei et al. 2001; Unsworth et al. 2005), reflecting bright spots (Brown et al. 1996; Makovsky et al. 1996) and high heat flow (Francheteau et al. 1984) attest to the presence of partial melting and/or aqueous fluids in the middle and/or lower crust of the southern Tibet. The focus of debate is whether the partial melting and the related low seismic velocity bulks are pervasive or isolated. To solve this
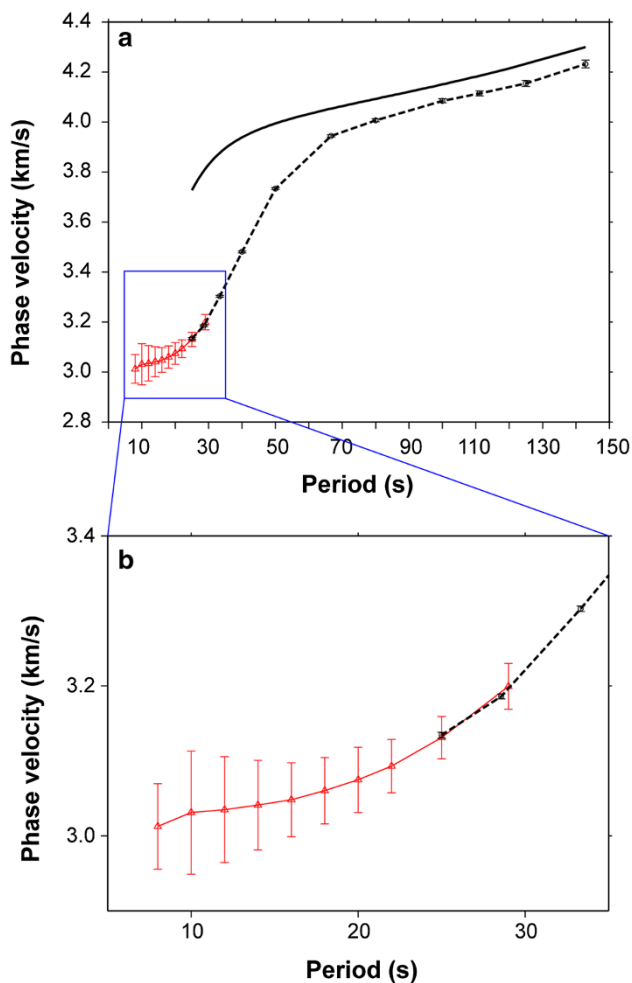
**Fig. 5 a** Average Rayleigh wave phase velocities in the southern Tibet. *Red curve* with *triangles* is the result of ambient noise tomography in this paper. *Black dashed curve* with *circles* is the result of two-plane wave tomography (Jiang et al. 2011). *Black solid curve* is the synthetic dispersion curve of the global AK135 model. The uncertainties are also plotted as *error bars*. **b** Figure zoomed in at the primary period of ambient noise tomography. At the overlapped period, the phase velocities are almost equal in between ambient noise tomography and two-plane wave tomography



**Fig. 6** Maps of Rayleigh wave phase velocity anomalies at the periods of 10–25 s. The velocity anomalies are calculated relative to the average velocities (Fig. 5). The *black triangles* denote the seismic stations. The main tectonic boundaries and the north–south trending rift zones are marked with the abbreviations as the same as that in Fig. 1

problem, we combine the results of ambient noise tomography in this paper (Fig. 6) and the previous results of two-plane wave tomography (Fig. 9), and construct an integrated image from the upper crust to mantle lithosphere.

Compiling the 2D phase velocity maps at the periods of 10–142 s (Figs. 6, 9) and the sensitivity functions of phase velocities to S-wave velocities (Fig. 7), we find that the low velocity bulks are primarily restricted to the rift zones (e.g., TYR and YGR) within the depth range of lithosphere. However, low velocities are prevailing in the mid-crust of southern Tibet. Our results are consistent with the previous results of Hung et al. (2010) that the low velocity bulks in the lower crust are not interconnected. Furthermore, our results show important evidence that the pervasive low
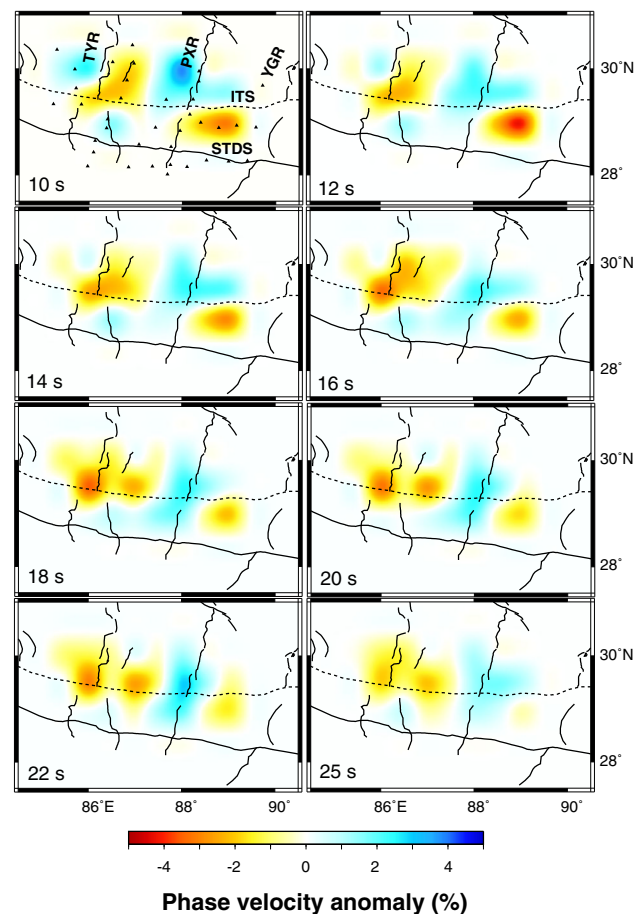
velocities and related crustal channel flow are possibly present in the middle crust of the southern Tibet.

As the observed low velocities are mainly restricted to the rift zones in the lithosphere of southern Tibet, except for in the middle crust, its distribution may provide some insights to the formation of the salient north–south trending rift zones here. Previous studies tended to interpret that the rift zones were just restricted to the upper crust based on the analysis of rift flank topography (Masek et al. 1994). Geophysical implications of a very weak mid-crust according to the pervasive low velocities also supported this interpretation (Cogan et al. 1998; Nelson et al. 1996). However, Yin (2000) proposed that a coherent rifting was needed throughout the entire crust and mantle lithosphere based on the instability analysis of rift spacing. The ultrapotassic and adakitic magmatism along the rift zones also reflected the rift zones that may cut down into the lower crust and even mantle lithosphere (Williams et al.
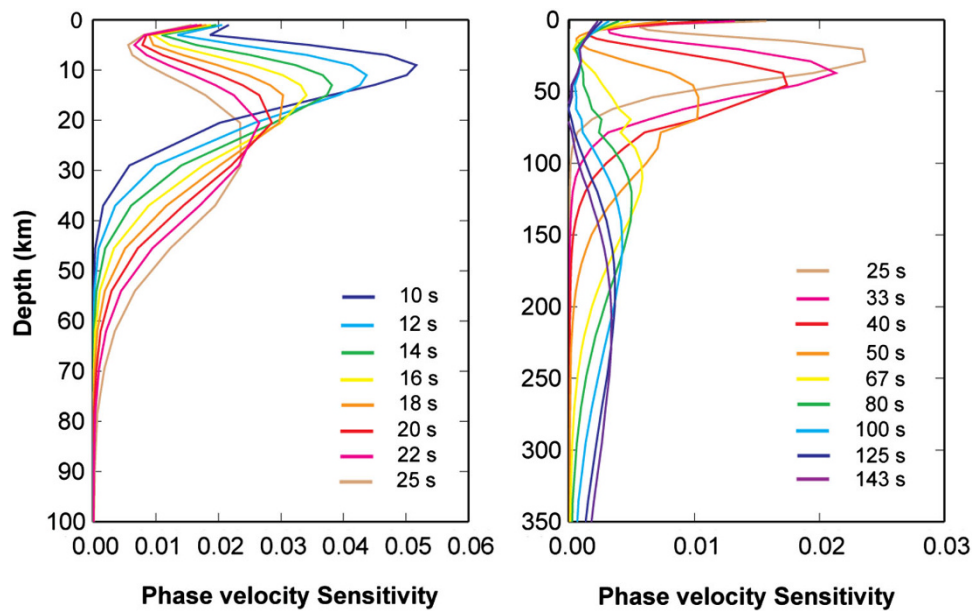
**Fig. 7** Rayleigh wave phase velocity sensitivity kernels to the 1D average shear wave velocity model in southern Tibet. **a** The kernels at the short periods. **b** The kernels at the long periods
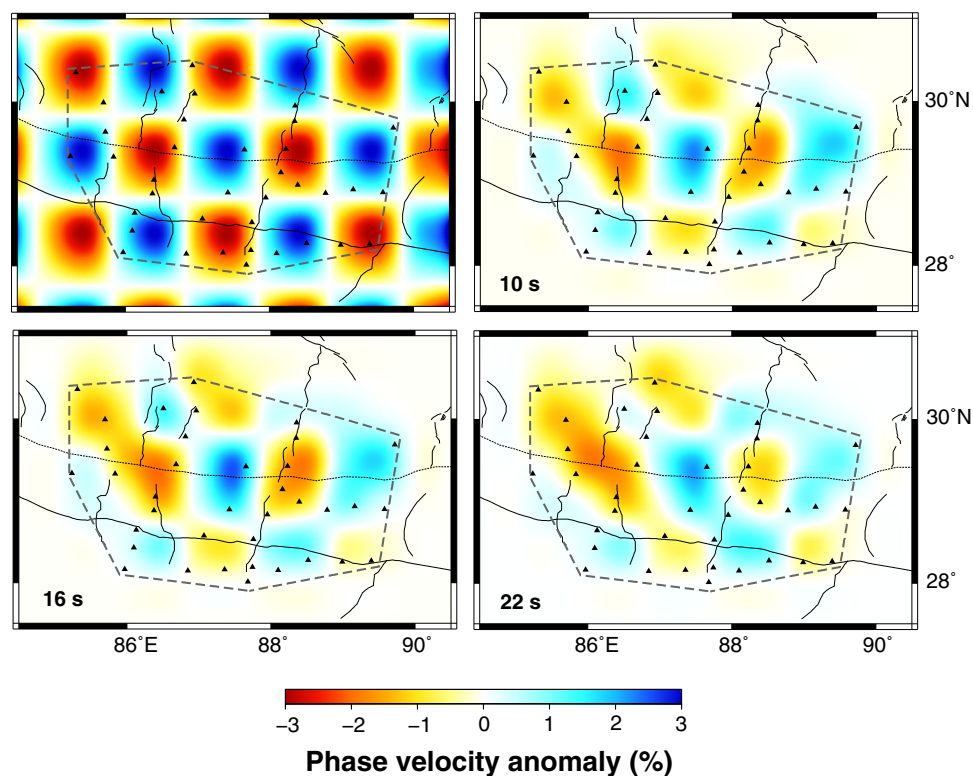


**Fig. 8** Checkerboard tests for the inversion of phase velocities. **a** Input model with ±3 % anomaly amplitude and 100 km anomaly size. **b–d** Recovered models at 10, 16, 22 s. The windows drawn by *dashed lines* delineate the reliable area in the inversion. The *black triangles* denote the seismic stations. The main tectonic boundaries and the N–S trending rifts are marked with the abbreviations as the same as that in Fig. 1

2001; Chung et al. 2005). Recent body wave tomography studies provided the direct evidences that low velocities were present from the lower crust to the upper mantle along the rift zones (Ren and Shen 2008; Hung et al. 2010; Liang et al. 2011, 2012). The contradictory observations also occur in our compiled results. The pervasive low velocities
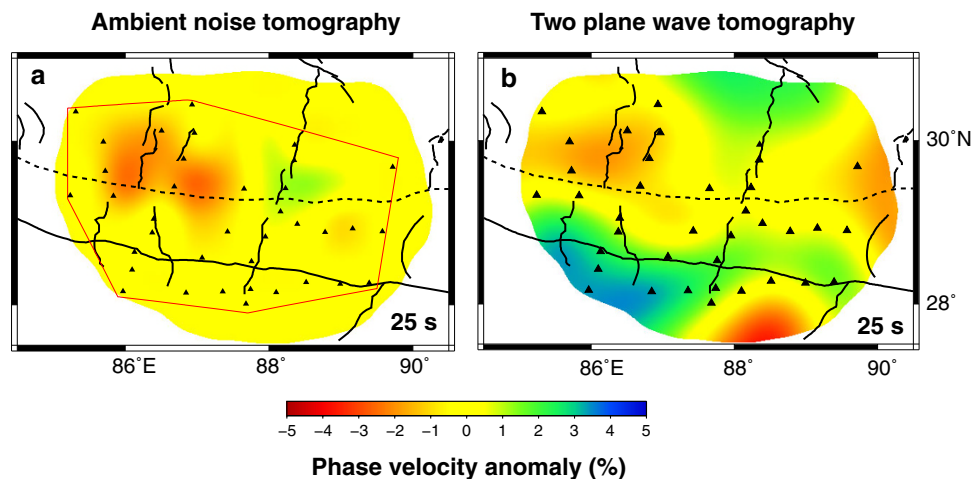
**Ambient noise tomography**          **Two plane wave tomography**



**Fig. 9** Comparison of phase velocity maps at 25 s between ambient noise tomography (**a**) and two-plane wave tomography (**b**). The result of two-plane wave tomography is from Jiang et al. (2011). The reliable regions of two types of tomographic results are plotted. The *black triangles* denote the seismic stations. The main tectonic boundaries and the north–south trending rift zones are marked with the abbreviations as the same as that in Fig. 1
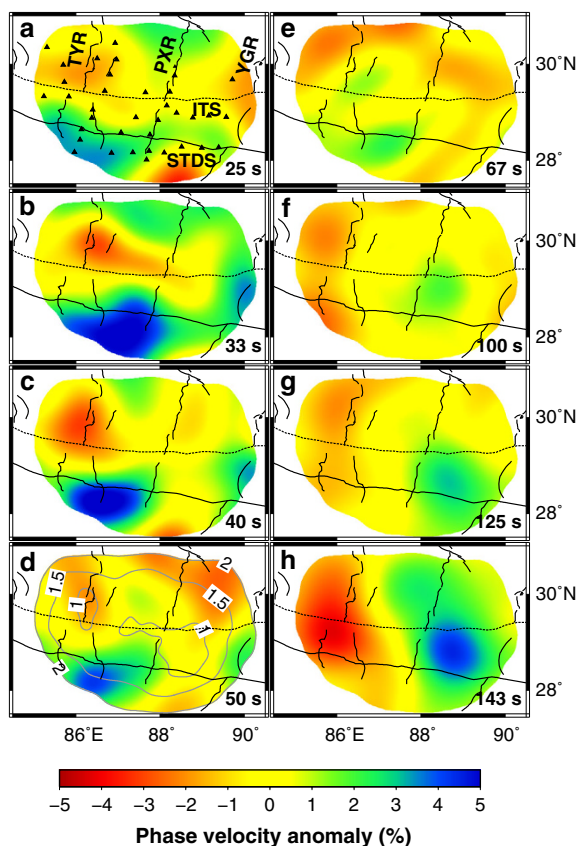


**Fig. 10** Maps of Rayleigh wave isotropic phase velocity anomalies and standard derivations (Jiang et al. 2011). The phase velocity anomaly maps are illustrated at the periods of **a** 25 s, **b** 33 s, **c** 40 s, **d** 50 s, **e** 80 s, **f** 100 s, **g** 125 s, and **h** 143 s. The velocity anomalies are calculated relative to the average phase velocities in the entire study region. The maps are clipped using the contour of 2 per cent double standard errors at the period of 50 s in **d**. The *black triangles* denote the seismic stations in (**a**). The main tectonic boundaries and the N–S trending rifts are marked with the abbreviations as the same as that in Fig. 1

in the mid-crust suggest the decoupling between the upper crust and the deep lithosphere. It seems to support that the rift zones are restricted within the upper crust. However, the sustained low velocities are observed from the upper crust to the bottom of lithosphere just beneath the rift zones. We imply that some of the rift zones should originate from a very deep source. This paradox could not be solved simply by the distribution of low velocity bulks identified by geophysical observations.

Compiling the geochemical and geochronological studies on the igneous rocks in the southern Tibet with our results, we establish a possible geodynamic process that reconciles the paradox mentioned above. Both our surface wave tomography and the previous body wave tomography (Ren and Shen 2008; Hung et al. 2010; Liang et al. 2011, 2012) observed the low velocities extending throughout the lithosphere. The mechanisms of deep earthquake in the lower crust to mantle lithosphere also showed east–west extension stress status in the lithosphere of southern Tibet (Chen and Molnar 1983; Zhu and Helmberger 1996; Chen and Yang 2004). The geochemical analysis of the igneous rocks exposed along the rift zones identified a deep magma source in the lower crust to mantle lithosphere (Williams et al. 2001; Chung et al. 2005). All these evidences refer to a rifting process of the whole lithosphere in the southern Tibet (Fig. 10a). According to the geochronological studies on these igneous rocks, the rifting of the whole lithosphere may begin in Miocene (~26–10 Ma). The surface geological survey of the rift zones gave the starting age of rifting later than ~8 Ma (Harrison et al. 1995; Yin et al. 1999; Mahéo et al. 2007). And their related conclusion was that the rift zones were restricted to the upper crust. Therefore, we present a possible two-stage scenario of the formation of the north–south trending rift zones in the
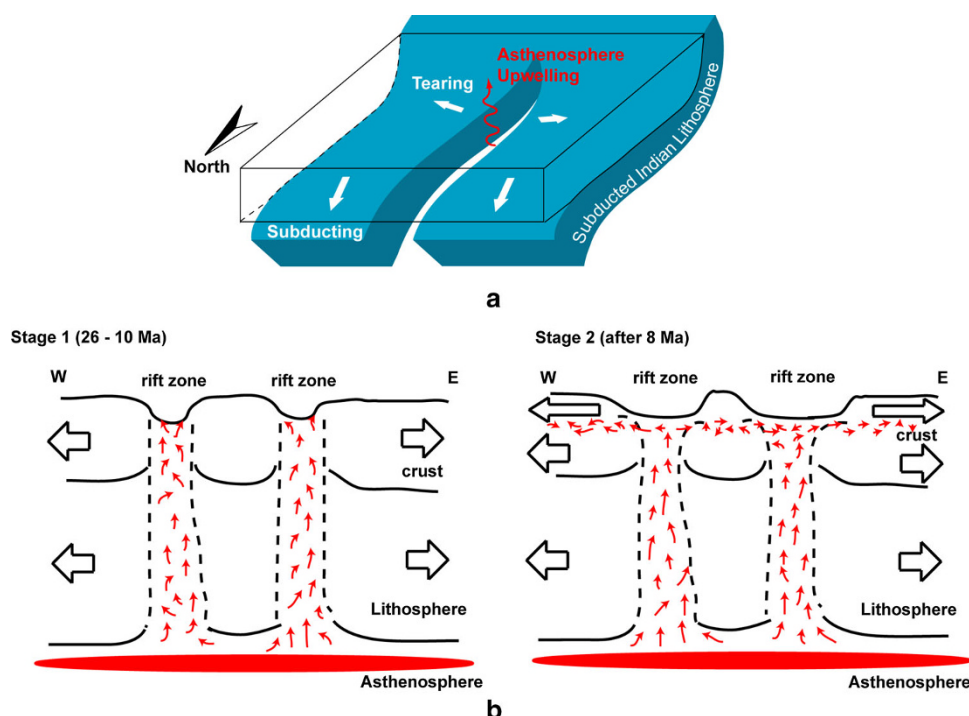
**Fig. 11** Cartoon of the formation of north–south trending rift zones. **a** 3D view at present **b** two stages of formation on time scale

southern Tibet as follows (Figs. 10b). In the early stage (∼26–10 Ma), the subducted Indian lithosphere broke. It caused the coherent rifting throughout the entire lithosphere (Fig. 11). In the late stage (after ∼8 Ma), the upwelling hot materials expanded in the middle crust and caused the decoupling between the upper crust and the deep lithosphere. The rifting near the Earth's surface became salient than the deep structure did. Thus, the geological history of the rift zones is closely associated with the deformation or break of the entire lithosphere.

## 5 Conclusions

We have preformed the ambient noise tomography in the southern Tibet with the data collected by a 2D seismic array of Hi-CLIMB project. 2D phase velocity maps at the short periods of 10–25 s are established. Combined with the previous study of two-plane-wave teleseismic tomography, we present a integrated image of the lithosphere in the southern Tibet. According to the relationship between the depth and the period of Rayleigh wave, we imply that the low velocities are mainly confined along some of the rift zones in the lithosphere of southern Tibet. An exception is that the pervasive low velocities are identified in the mid-crust of both the rift zones and the regions outside of the rift zones. To interpret the observations, we compiled the studies of geophysics, geochemistry, and geochronology, and present a two-stage scenario on the formation of the rift zones.

## References

Barmin MP, Ritzwoller MH, Levshin AL (2001) A fast and reliable method for surface wave tomography. Pure Appl Geophys 158:1351–1375

Beaumont C, Jamieson RA, Nguyen MH, Medvedev S (2004) Crustal channel flows: 1. Numerical models with applications to the tectonics of the Himalayan-Tibetan orogen. J Geophys Res 109(B06406):2003J. doi:10.1029/B002809

Bensen GD, Ritzwoller MH, Barmin MP, Levshin AL, Lin F, Moschetti MP, Shapiro NM, Yang Y (2007) Processing seismic ambient noise data to obtain reliable broad-band surface wave dispersion measurements. Geophys J Int 169:1239–1260. doi:10.1111/j.1365-246X.2007.03374.x

Brown LD, Zhao W, Nelson KD, Hauck M, Alsdorf D, Ross A, Cogan M, Clark M, Liu X, Che J (1996) Bright spots, structure, and magmatism in southern Tibet from INDEPTH seismic reflection profiling. Science 274:1688–1690

Chen W-P, Molnar P (1983) Focal depths of intracontinental and intraplate earthquakes and their implications for the thermal and mechanical properties of the lithosphere. J Geophys Res 88:4183–4214

Chen W-P, Yang Z (2004) Earthquakes beneath the Himalayas and Tibet: evidence for strong lithospheric mantle. Science 304:1949–1952. doi:10.1126/science.1097324

Chen LH, Booker JR, Jones AG, Wu N, Unsworth MJ, Wei WB, Tan HD (1996) Electrically conductive crust in southern Tibet from INDEPTH magnetotelluric surveying. Science 274:1694–1696

Chung S-L, Chu M-F, Zhang Y, Xie Y, Lo C-H, Lee T-Y, Lan C-Y, Li X, Zhang Q, Wang Y (2005) Tibetan tectonic evolution inferred from spatial and temporal variations in post-collisional magmatism. Earth Sci Rev 68:173–196

Cogan MJ, Nelson KD, Kidd WSF, Wu C, Project INDEPTH Team (1998) Shallow structure of the Yadong-Gulu rift, southern Tibet, from refraction analysis of Project INDEPTH common midpoint data. Tectonics 17:46–61

Cotte N, Pedersen H, Campillo M, Mars J, Ni JF, Kind R, Sandvol E, Zhao W (1999) Determination of the crustal structure in southern Tibet by dispersion and amplitude analysis of Rayleigh waves. Geophys J Int 138:809–819

Francheteau J, Jaupart C, Shen XJ, Kang WH, Lee DL, Bai JC, Wei HP, Deng HY (1984) High heat-flow in southern Tibet. Nature 307:32–36

Harrison TM, Copeland P, Kidd WSF, Lovera O (1995) Activation of the Nyainqentanghla shear zone: implications for uplift of the southern Tibetan Plateau. Tectonics 14:658–676

Hung S-H, Chen W-P, Chiao L-Y, Tseng T-L (2010) First multi-scale, finite- frequency tomography illuminates 3D anatomy of the Tibetan Plateau. Geophys Res Lett 37:L06304. doi:10.1029/2009GL041875

Jiang MM, Zhou SY, Sandvol E, Chen XF, Liang XF, Chen YJ, Fan WY (2011) 3D lithospheric structure beneath southern Tibet from Rayleigh-wave tomography with a 2D seismic array. Geophys J Int 185:593–608

Kennett BLN, Engdahl ER, Buland R (1995) Constraints on seismic velocities in the Earth from travel-times. Geophys J Int 122:108–124

Kind R, Ni J, Zhao W, Wu J, Yuan X, Zhao L, Sandvol E, Reese C, Nabelek J, Hearn T (1996) Evidence from earthquake data for a partially molten crustal layer in southern Tibet. Science 274:1692–1694

Levshin AL, Yanovskaya TB, Lander AV, Bukchin BG, Barmin MP, Ratnikova LI, Its EN (1989) In: Keilis-Borok VI (ed) Seismic surface waves in a laterally inhomogeneous earth. Kluwer, Norwell

Liang X, Shen Y, Chen YJ, Ren Y (2011) Crustal and mantle velocity models of southern Tibet from finite frequency tomography. J Geophys Res 116:B02408. doi:10.1029/2009JB007159

Liang XF, Sandvol E, Chen YJ, Hearn T, Ni J, Klemperer S, Shen Y, Tilmann F (2012) A complex Tibetan upper mantle: a fragmented Indian slab and no south-verging subduction of Eurasian lithosphere. Earth Planet Sci Lett 333:101–111

Lobkis OI, Weaver RL (2001) On the emergence of the Green's function in the correlations of a diffuse field. J Acoust Soc Am 110:3011–3017

Mahéo G, Leloup PH, Valli F, Lacassin R, Arnaud N, Paquette J-L, Fernandez A, Haibing L, Farley KA, Tapponnier P (2007) Post 4 Ma initiation of normal faulting in southern Tibet. Constraints from the Kung Co half graben. Earth planet Sci Lett 256:233–243

Makovsky Y, Klemperer SL, Ratschbacher L, Brown LD, Li M, Zhao WJ, Meng FL (1996) INDEPTH wide-angle reflection observation of P-wave-to-S-wave conversion from crustal bright spots in Tibet. Science 276:1690–1691

Masek JG, Isacks BL, Fielding EJ, Browaeys J (1994) Rift flank uplift in Tibet: evidence for a viscous lower crust. Tectonics 13:659–667

Nábelek J, Hetényi G, Vergne J, Sapkota S, Kafle B, Jiang M, Su H, Chen J, Huang BS and Hi-CLIMB Team (2009). Underplating in the Himalaya-Tibet collision zone revealed by the Hi-CLIMB experiment. Science 325:1371. doi:10.1126/science.1167719

Nelson KD, Zhao W, Brown LD, Kuo J, Che J, Liu X, Klemperer SL, Makovsky Y, Meissner R, Mechie J, Kind R, Wenzel F, Ni J, Nabelek J, Leshou C, Tan H, Wei W, Jones AG, Booker J, Unsworth M, Kidd WSF, Hauck M, Alsdorf D, Ross A, Cogan M, Wu C, Sandvol E, Edwards M (1996) Partially molten middle crust beneath southern Tibet: synthesis of project INDEPTH results. Science 274:1684–1688

Pham VN, Boyer D, Therme P, Yuan XC, Li L, Jin GY (1986) Partial melting zones in the crust in southern Tibet from magnetotelluric results. Nature 319:310–314

Rapine R, Tilmann F, West M, Ni J, Rodgers A (2003) Crustal structure of northern and southern Tibet from surface wave dispersion analysis. J Geophys Res 108:2120. doi:10.1029/2001JB000445

Ren Y, Shen Y (2008) Finite frequency tomography in southeastern Tibet: evidence for the causal relationship between mantle lithosphere delamination and the north-south trending rifts. J Geophys Res 113:B10316. doi:10.1029/2008JB005615

Roux P, Sabra KG, Kuperman WA, Roux A (2005) Ambient noise cross correlation in free space: theoretical approach. J Acoust Soc Am 117:79–84

Royden LH, Burchfiel BC, van de Hilst RD (2008) The geological evolution of the Tibetan plateau. Science 321:1054. doi:10.1126/science.1155371

Unsworth MJ, Jones AG, Wei W, Marquis G, Gokarn SG, Spratt JE and the INDEPTH-MT team (2005) Crustal rheology of the Himalaya and southern Tibet inferred from magnetotelluric data. Nature 438:78–81. doi:10.1038/nature04154

Wei W, Unsworth M, Jones A, Booker J, Tan H, Nelson D, Chen L, Li S, Solon K, Bedrosian P, Jin S, Deng M, Ledo J, Kay D, Roberts B (2001) Detection of widespread fluids in the Tibetan crust by magnetotelluric studies. Science 292:716–718

Williams HM, Turner SP, Kelley SP, Harris NBW (2001) Age and composition of dikes in southern Tibet: new constrains on the timing of east–west extension and its relationship to postcollisional volcanism. Geology 29:339–342

Yang Y, Ritzwoller MH, Lin F-C, Moschetti MP, Shapiro NM (2008) Structure of the crust and uppermost mantle beneath the western United States revealed by ambient noise and earthquake tomography. J Geophys Res 113:B12310. doi:10.1029/2008JB005833

Yao H, Van Der Hilst RD, de Hoop MV (2006) Surface-wave array tomography in SE Tibet from ambient seismic noise and two-station analysis. I. Phase velocity maps. Geophys J Int 166(732–744):2006. doi:10.1111/j.1365-246X.03028.x

Yao H, Beghein C, Van Der Hilst RD (2008) Surface wave array tomography in SE Tibet from ambient seismic noise and two-station analysis. II. Crustal and upper-mantle structure. Geophys J Int 173:205–219. doi:10.1111/j.1365-246X.2007.03696.x

Yin A (2000) Mode of Cenozoic east–west extension in Tibet suggesting a common origin of rifts in Asia during the Indo-Asian collision. J Geophys Res 105:21745–21759

Yin A, Kapp P, Murphy M, Manning CE, Harrison TM, Ding L, Deng X, Wu C (1999) Significant late Neogene east–west extension in north Tibet. Geology 27:787–790

Zhu L, Helmberger D (1996) Intermediate depth earthquakes beneath the India-Tibet collision zone. Geophys Res Lett 23:435–438. doi:10.1029/96GL00385